



ELSEVIER

Contents lists available at ScienceDirect

Nuclear Instruments and Methods in Physics Research A

journal homepage: www.elsevier.com/locate/nima

Micro-channel plates and vacuum detectors



T. Gys*

CERN, PH Department, CH-1211 Geneva 23, Switzerland

ARTICLE INFO

Available online 18 December 2014

Keywords:

Image intensifier tubes
Scintillating fiber tracking detectors
Particle identification and time-of-flight detectors

ABSTRACT

A micro-channel plate is an array of miniature electron multipliers that are each acting as a continuous dynode chain. The compact channel structure results in high spatial and time resolutions and robustness to magnetic fields. Micro-channel plates have been originally developed for night vision applications and integrated as an amplification element in image intensifiers. These devices show single-photon sensitivity with very low noise and have been used as such for scintillating fiber tracker readout in high-energy physics experiments. Given their very short transit time spread, micro-channel plate photomultiplier tubes are also being used in time-of-flight and particle identification detectors. The present paper will cover the history of the micro-channel plate development, basic features, and some of their applications. Emphasis will be put on various new manufacturing processes that have been developed over the last few years, and that result in a significant improvement in terms of efficiency, noise, and lifetime performance.

© 2014 CERN for the benefit of the Authors. Published by Elsevier B.V. This is an open access article under the CC BY license (<http://creativecommons.org/licenses/by/4.0/>).

1. Introduction

The development of conventional photomultiplier tubes (PMTs) was started in the 1930s. In these vacuum devices, single photons are converted in photoelectrons by a photocathode. This charge is amplified by a chain of discrete dynodes to a level matching the sensitivity of standard electronics. Dynodes are basically structures emitting secondary electrons when hit by primary charged particles, low-energy electrons in the present case. In PMTs, the dynodes are each operated at increasing bias voltage and through repeated secondary electron emission processes, charge signal amplification occurs. Various dynode configurations exist: linear, cage, venetian blind, box-and-grid, fine mesh, etc. The complexity of their mechanics and biasing circuitry makes them difficult to fabricate; it does not allow for compact structures that would be more robust in e.g. magnetic field environments. In the late 1990s, the metal channel dynode technology allowed for the fabrication of more compact PMTs. These devices essentially maintain the performance of conventional tubes, in particular their single photon sensitivity. They can be segmented in arrays of typically 8×8 or 16×16 mm-size elementary cells. They are however not suited for applications where very high spatial ($\leq 50 \mu\text{m}$) and/or timing (≤ 50 ps) resolutions are required. In this case, alternative technologies for photon detection and amplification based on micro-channel plates (MCPs) may be exploited.

The present paper will cover the history of the MCP development, some of the MCP basic features, and applications in high-energy physics. Emphasis will be put on various new MCP manufacturing processes that have been developed over the last few years and that result in a significant improvement in terms of efficiency, noise, and lifetime performance.

2. History

2.1. The channel electron multiplier

The concept of a continuous dynode for the multiplication of electrons was proposed for the first time by Farnsworth [1]. His apparatus essentially consisted of two devices encapsulated in an evacuated glass envelope (Fig. 1). The first device was generating a modulated electron stream that was subsequently collimated and directed towards a second device acting as an amplification stage. The key elements of that stage were a hollow resistor and a filamentary electrode coated with a secondary emitter material (Th or Ba) and extending axially of the resistor. By a potential applied across the resistor, a graduated longitudinal electrostatic field is produced. Prior to active operation, the filament is heated up to incandescence; the secondary emitter material is vaporized from the filament surface and deposited onto the inner surface of the resistor. During active operation, as the primary electron stream is striking the resistor inner surface, secondary electrons are created. They are accelerated longitudinally by the graduated electrostatic field but also transversally by the filament supplied with an appropriate bias voltage. These electrons

* Corresponding author. Tel.: +41 22 767 8307; fax: +41 22 766 8640.
E-mail address: Thierry.Gys@cern.ch

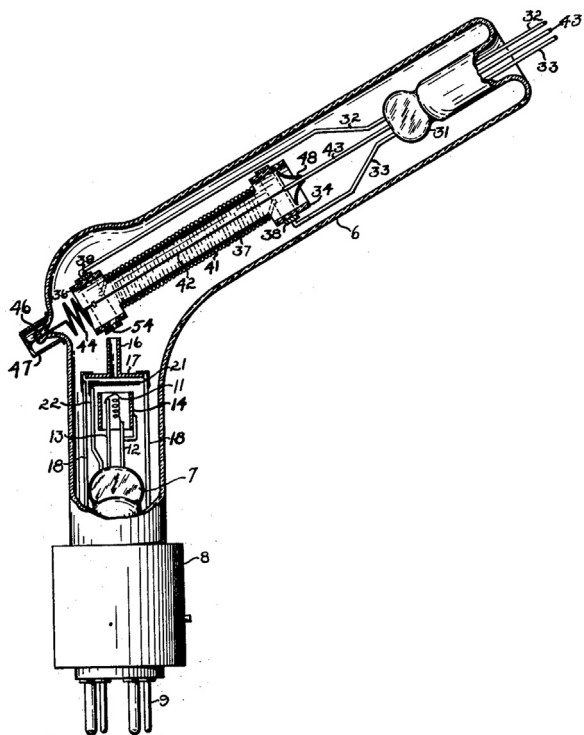


Fig. 1. The first channel electron multiplier developed by Farnsworth [1].

hit the opposite resistor surface, causing again a release of additional secondary electrons. This effect is repeated and contributes to the overall electron amplification process. This first electron multiplier proved to be linear up to the point where space charge effects started to dominate.

Further implementations of electron multipliers were delayed until the early 1960s, when much experience on secondary electron emission had been acquired [2] essentially through the development of PMTs. At the same period more suitable materials became available. More particularly, earlier work by Green and Blodgett [3,4] showed that after appropriate hydrogen treatment at high temperature, lead silicate glass exhibits the properties of electrical conductivity and secondary emission.

The original concept of Farnsworth was improved by Oshchekpov et al. [5]. These authors described the operation of a simpler electron multiplier based on the same principle of continuous secondary electron amplification, but without central focussing electrode. For the inner channel coating, a mixture of TiO_2 and MgO was found to satisfy the conductivity, secondary emission yield and stability requirements. The complete fabrication process including the preparation of a ceramic tube was detailed. Systematic studies of the secondary emission coefficient, multiplier gain and output current in function of the applied voltage were carried out. Finally, these authors introduced the parameter α as the ratio between channel length and diameter. It turns out that most of the electrical performance of electron multipliers depends on α . As will be seen below, this characteristic opened the way to any dimensional reduction of the electron multiplier as soon as the technology would permit.

Heroux and Hinteregger [6] developed a windowless resistance strip magnetic electron multiplier for the detection of extreme ultraviolet radiation. Based on a planar geometry, the device consisted of dynode and field strips made of glass and internally coated with high-resistance tin oxide and antimony. Appropriate external voltages establish an electric field between the strips and voltage gradients along both strips. A magnetic field is applied perpendicular to the electric field and parallel to the strip surfaces. These crossed magnetic

and electric fields result in secondary electrons refocussing on the dynode strip and producing secondary electrons. Through the repetition of this process, current amplification is achieved. With this magnetic electron multiplier, DC gains up to 10^8 have been measured.

A similar magnetic electron multiplier development was carried out by Goodrich and Wiley [7]. Their device structure subsequently evolved towards very small, tubular continuous dynode channels [8]. At their metallized ends was applied a potential of 1 to 2 kV and no magnetic field was required. By grouping these channels in parallel arrays, current density distributions could be determined. This paved the way towards potential applications that include image intensification. It was also confirmed experimentally that for a constant parameter α and channel diameters ranging from 0.04 to 0.004 in, the same high gains were achieved.

The principle and basic characteristics of channel electron multipliers (CEMs) have been thoroughly described in the literature [9–11]. They will not be discussed in detail in the present paper. One important and detrimental effect to be mentioned however is ion feed-back that may become important at high gains ($\geq 10^5$). The charge pulse at the channel output may create residual gas ions. These are accelerated back toward the channel input where they may produce further secondary electrons that are in turn multiplied. The consequences of ion feed-back are multiple: the primary output charge pulse is followed by smaller ones, the channel capacity is decreased and the device lifetime is directly affected. One way to mitigate these ion feed-back effects is to curve the channel. With this geometry, an ion will strike the channel wall at lower energies and the probability to generate secondary electrons is decreased. Curved channels are however difficult to assemble in arrays. The ultimate gain limit with curved channels is driven by space-charge effects near the output [12–14].

Single CEMs are robust and efficient detectors of positive and negative ions as well as electrons and photons. Various CEM models suited for specific applications e.g. in space and mass spectrometry are available on the market. An early example of application is the work of Johnson [15]. The performance of a curved CEM was assessed in the vacuum ultraviolet range (300–1700 Å) where the CEM detection efficiency was seen to be similar to that of tungsten. Green et al. [16] exploited the fast-timing characteristics of some CEMs by measuring half-lives of nuclear levels in ^{59}Co and ^{170}Yb with a precision of 20 ps.

2.2. The micro-channel plate

As mentioned in the previous section, the fundamental electrical characteristics of a CEM basically depend on the length-to-diameter ratio α . Consequently, the channel size can be reduced to a limit set by the technology, and a number of these channels can be bonded together to form an array with imaging capability. The very first MCPs were assembled with many single small-diameter CEMs bonded together [11]. This rather rudimentary process was superseded by fiber drawing techniques. These originally made use of hollow channels that have subsequently been replaced with “billets” having etchable glass core and non-etchable glass cladding. The manufacturing steps are as follows [10,11]. The billets are heated and drawn down to typically 0.8 mm diameter fibers. Thousands of such fibers are bundled together to form a hexagonal rod. The rod is drawn again and several such rods are fused together to form a MCP “boule”. The boule is sliced in MCP wafers that are further polished and chemically etched (Fig. 2). Individual MCPs are heated under reducing hydrogen atmosphere to provide electrical conductivity and secondary emission. Typical surface resistivity values for such treated glass reach 10^7 to $10^{13} \Omega/\square$; the latter figure corresponds to a typical MCP resistance of $10^9 \Omega$. Electrodes generally made of NiCr are deposited on the MCP input and output faces. The MCPs finally undergo pre-conditioning through electron scrubbing in order to stabilize their operation.

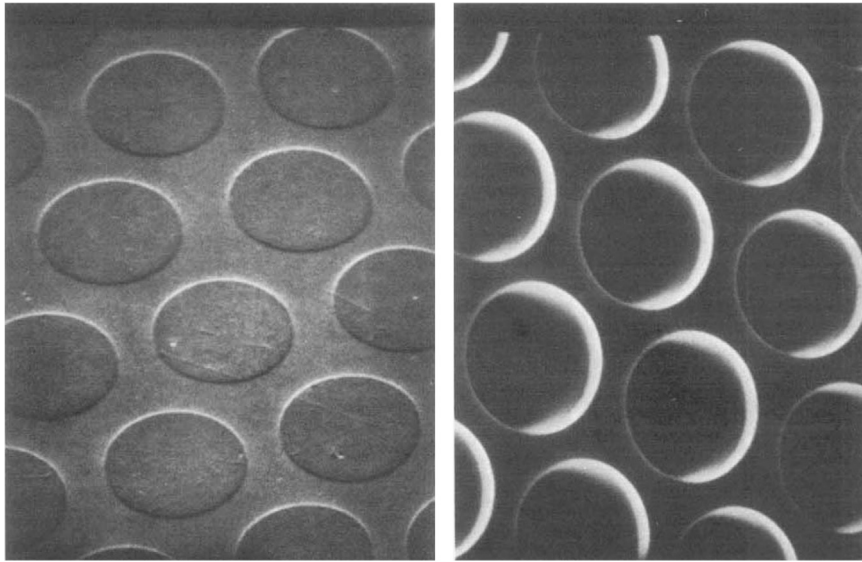


Fig. 2. Scanning electron microscope photographs of an MCP before (left) and after (right) chemical etching and processing [10].

Numerous papers on general [10,11] and specific [17–19] MCP aspects are available in the literature. Some basic MCP features and characteristics are listed in the following.

The main MCP geometrical parameters are:

- Pore diameter d : 6–25 μm ;
- Channel length L : 400–1000 μm ;
- Diameter-to-length ratio $\alpha = L/d$: 40–100;
- Open-area-ratio: 55–65%.

For single straight-channel MCPs, the typical gain is in the range 10^3 – 10^4 . Similarly to straight CEMs, this MCP configuration is limited by ion feed-back effects. The pulse height distribution approximates a negative exponential. As previously mentioned already, ion feed-back is essentially suppressed in curved-channel MCPs in which the gain is only limited by space charge effects when a dynamic equilibrium is reached. The pulse height distribution is quasi Gaussian. These attractive features are however counterbalanced by the difficulty to fabricate small-size curved-channel MCPs.

A high-gain space-charge saturated output pulse can be achieved by a stack of two straight-channel MCPs where the bias angle is alternated. This prevents positive ions produced at the output of the rear plate from reaching the front plate. In this so-called “Chevron” configuration, typical gains are in the range 10^6 – 10^7 . The resulting pulse height distribution is a peak with a resolution that improves by decreasing the separation between the two plates and by increasing the inter-plate bias voltage [10]. Similarly to the Chevron configuration, the stacking of three MCPs is also possible and is referred to as the Z-stack configuration [11].

3. Micro-channel plates for low-light level imaging

3.1. Second generation image intensifier tubes

Micro-channel plates were originally developed for night vision applications mainly in the military domain [20]. They were integrated as a high-gain and high-resolution element in proximity-focused image intensifiers commonly called second-generation (Gen II) image tubes.

The former image tube generation (Gen I) used a photocathode and a cross-focusing electron optics that was directly accelerating and imaging photoelectrons onto a phosphor screen. This resulted

in typical gains of order 10^3 . In Gen I tubes, the output image suffered from optical distortions inherent to the electron-optics design. On the contrary, Gen II tubes provide larger amplifications in the range 1 – 2×10^4 and distortion-free images. From their design, Gen II tubes are also light-weight and compact devices. For some specific applications, the phosphor screen is deposited onto an optical fiber output window that maintains the spatial resolution. This fiber window can possibly be tapered to match the size of e.g. a CCD readout chip (Fig. 3).

One key aspect of Gen II image intensifiers is their spatial resolution [20,22]. The input photon energy and photocathode threshold will determine the emission velocity range of primary photoelectrons and their resulting transverse deviation during their transit to the MCP. The energy distribution of output electrons after MCP amplification is also affecting the spatial resolution [23]. Electron backscattering may occur at the MCP input and at the output screen, generating image halos [24]. Mitigating all these effects primarily requires small gaps between the photocathode and the MCP input face (typically 200 μm or less) and between the MCP output face and the output screen (typically 1 mm). Additionally, end spoiling of the MCP output electrode [25] contributes to a better collimation of the output electrons. End spoiling refers to the depth of penetration d_{es} of the output electrode deposition into the channel ends. An optimal compromise between better spatial resolution and acceptable gain decrease results in d_{es} in the range of one to two times the micro-channel diameter d . Hoenderken et al. [26] have however shown that electrostatic lensing effects induced by end-spoiling should not be neglected, and their contribution to the spatial resolution might in certain cases become dominant.

3.2. Scintillating fiber trackers in high-energy physics

In the years 1980s–1990s, a whole generation of charged-particle trackers in high-energy physics experiments was based on scintillating fibers (SciFi) [27–30]. The requirements of optimal area coverage, sensitivity to single photons and high spatial resolution were satisfied by readily-available image intensifiers. The different fiber layers were grouped, bundled and coupled to an optoelectronic readout chain consisting of a combination of various image intensifier types. The first stage was a Gen I tube that has large input coverage and collection efficiency close to 100%. This tube was equipped with electron optics de-magnifying the input image to a size matching that of one (or more) proximity-focused

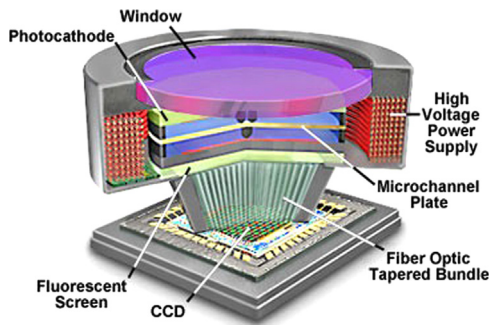


Fig. 3. Schematic 3D view of a second-generation image intensifier tube equipped with a micro-channel plate [21].

tubes of which at least one was a high-gain Gen II tube. The final stage (if any) was another, smaller Gen I tube de-magnifying the image to a size compatible with the size of a CCD chip eventually recording the particle track image. Electrostatic tubes are more sensitive to magnetic fields. Consequently, the readout chain, generally located at the tracking detector periphery, was shielded with adequate ferromagnetic material.

Such a SciFi tracker was developed and built as part of the upgrade of the UA2 central detector [27,28]. One of the main physics motivations for this upgrade was the search for electrons with transverse momentum in the range 10–30 GeV/c as a signature for top quark production. This required improved electron identification and a new cylindrical vertex detector, fitting inside the existing central calorimeter. The SciFi tracker was an essential component of this new detector. With 1 mm-diameter fibers, an average detection efficiency of 88% per fiber layer was achieved. The standard deviation of the track residuals was 0.39 mm and the two-track resolution 3 mm [28].

The SciFi tracker of the CHORUS neutrino oscillation experiment followed the same philosophy [29,30]. In CHORUS, the search for ($\nu_\mu - \nu_\tau$) oscillations was based on the detection of the charged current reaction $\nu_\tau N \rightarrow \tau^- X$ in a background of ν_μ -induced interactions. Given the small decay length of the τ lepton ($c\tau = 90 \mu\text{m}$) a high-resolution, high-hit density target detector was chosen in the form of nuclear emulsions to identify the decay vertex. The role of the SciFi tracker was to restrict the search of the vertex location in the bulk emulsions. Fibers of 500 μm diameter were used. The intrinsic spatial resolution of the optoelectronic chain (including the CCD) ranged between 340 and 415 μm FWHM, while the track residuals showed a FWHM of 350 μm . Adding these values in quadrature resulted in a two-track resolution of about 500 μm .

In the WA84 experiment [31], the search for B and \bar{B} meson decays required the specific development of a small-diameter SciFi active target and an efficient high spatial resolution optoelectronic readout chain. A number of SciFi active targets were tested. A target made of PMP-doped polystyrene fibers, 30 μm in diameter, proved to be the most promising candidate. The optoelectronic chain was rather complex and used a bent and magnifying glass fiber taper, image intensifier tubes of various types, a long (2.5 m) glass-fiber image guide and a CCD readout chip. The first part of the chain was located in a high (1.8 T) magnetic field environment and utilized standard proximity-focussed image intensifier tubes axially aligned with the magnetic field. These tubes were not equipped with MCPs as their open area ratio would have dramatically reduced the overall detection efficiency. After image transport by the image guide outside the magnetic environment, the light was further amplified by the combination of Gen I, Gen II and Gen I tubes. The Gen II tube was providing most of the amplification and could be gated when a first-level trigger was satisfied. In this optoelectronic system, various sources of noise were identified [32], including backscattering effects

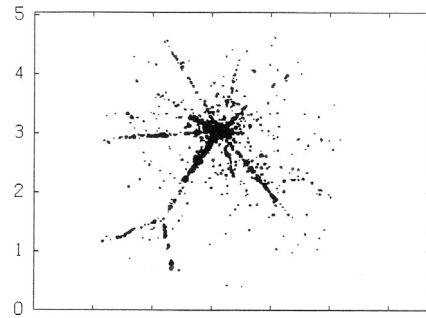


Fig. 4. Example of hadron interaction recorded by the WA84 experiment in a target made of 30 μm -diameter polystyrene fibers [31]. The horizontal and vertical scales (tick marks) are in mm.

already mentioned previously in this paper. The track residuals achieved with the 30 μm polystyrene fibers (Fig. 4) showed a standard deviation of 20 μm .

Nowadays speed requirements limit the use of standard image intensifiers in SciFi detectors, in particular because of their relatively slow phosphor screen and CCD readout. Novel, fast and efficient single photon detectors are available on the market in the form of avalanche photodiodes operated in Geiger mode. This readout technology will for instance be exploited in a new SciFi tracker currently under design and development for the LHCb upgrade [33].

4. Micro-channel plates for fast timing

4.1. Micro-channel plate photomultiplier tubes

The design, characteristics and performance of MCPs made them perfect candidates for compact PMTs with time resolutions better than what could be achieved with classical PMTs equipped with discrete dynodes. In the pioneering work of Boutot and Piétri [34], the design of a proximity-focused MCP-PMT was optimized for ultra-fast timing. The tube encapsulated a single MCP with 40 μm pore diameter. The output collector stage was a plane-circular anode integrated in a coaxial structure matching a 50 Ω transmission line. From exposure to ultra short (10 ps FWHM) pulses of a mode-locked laser, an overall transit time of 1 ns and a transit time spread (TTS) of less than 500 ps were measured.

Over the following two decades, numerous MCP-PMT developments and studies followed, resulting in ever improving performance. In particular, a TTS lower than 50 ps was achieved by MCPs with very small pore size in the range 6–12 μm . These results were reviewed by Fraser together with original contributions from the author in a comprehensive paper ([35] and references therein). The MCP gain, time resolution and robustness to magnetic field were discussed in detail. Analytical and numerical models were proposed and shown to be in good agreement with experimental results. The gain and lifetime aspects were also assessed. There is poor understanding about the basic mechanisms that induce an irreversible gain drop. It is suspected that changes in secondary electron yield and emission energy in the MCP lead-glass are closely related to the dose of electron bombardment. Recent developments improving MCP lifetime will be covered in Section 4.3.

Due to their intrinsic properties (narrow amplification channels and proximity focusing electron optics), MCP-PMTs are appropriate detectors for applications involving strong magnetic fields. In this environment, the MCP-PMT robustness is improved if their axis is aligned with the magnetic field direction and if small channel pore size is used [35]. Strong axial magnetic fields also improve the spatial resolution and reduce charge-sharing effects, an advantage in particular if the MCP-PMT tube is spatially segmented [36]. However, the

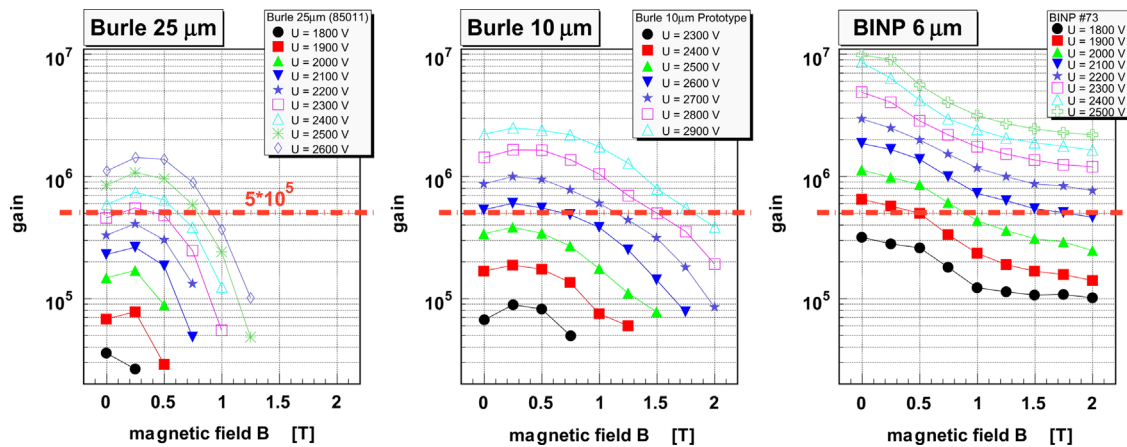


Fig. 5. Gain as a function of the magnetic field and for different high-voltage settings for MCP-PMTs developed by the PANDA Collaboration [38].

(possibly long) time tails induced by backscattering effects remain. Kichimi et al. [37] have compared the timing performance of MCP-PMTs (Chevron configuration and $6\ \mu\text{m}$ pore size) and fine-mesh PMTs in magnetic fields up to 1.5 T. Test results indicate that for both tube types, TTS values are rather stable against magnetic field strength and angle. In single photon mode, TTS values of 30 ps were measured for MCP-PMTs with marginal gain drop. Fine-mesh PMTs show TTS values of 140 ps up to 1 T. Beyond this field strength, their gain essentially drops to zero. More recent systematic MCP-PMT studies [38,39] established that for efficient single-photon detection, a pore diameter of $10\ \mu\text{m}$ or less is needed in a magnetic field up to 2 T. Both gain and time resolutions are best with a pore size of $6\ \mu\text{m}$ (Fig. 5).

4.2. Particle identification and time-of-flight detectors in high-energy physics

Over the last decade, a number of particle identification (PID) and time-of-flight (TOF) detectors have been proposed and developed for new, or for the upgrade of high-energy physics experiments. These detectors are based on the detection of Cherenkov light produced by charged particles in a quartz radiator. They follow the pioneer and successful concept realization and operation of the Babar DIRC (Detector of Internally Reflected Cherenkov light) [40].

In these experiments, the main requirements for the photon detectors are:

- Good overall area coverage;
- High single-photon detection efficiency optimized for Cherenkov light (blue and near UV region);
- High gain of typically 10^6 ;
- Spatial anode segmentation with typically mm pad size;
- Very high speed with typically single-photon TTS of order 50–100 ps;
- Robustness to magnetic field up to 2 T;
- Low noise;
- High photon rate capability for typical illumination levels $200\ \text{kHz}/\text{cm}^2$ up to $\geq 1\ \text{MHz}/\text{cm}^2$;
- Radiation hardness;
- Extended lifetime with marginal performance drop over 5–10 years of operation.

The basic requirements on gain, speed and B-field immunity are fulfilled by MCP-PMTs. Their area coverage has been dramatically improved through the availability of square-shaped tubes with reduced peripheral dead area. Photocathodes with improved quantum efficiency have also been developed and are now commercially

available. Manufacturer efforts were or are being made to provide the required level of anode segmentation. The most stringent requirement is device lifetime, directly related to gain and illumination levels. It will be discussed specifically in Section 4.3.

In the focusing DIRC (FDIRC) ([41] and references therein) photon detectors with relatively coarse anode segmentation of typically 5 mm are required to reconstruct the Cherenkov angle. The photon arrival time must be measured with a precision of 50–100 ps to correct for chromatic dispersion effects in the quartz radiator. This time resolution also helps in background suppression. A first FDIRC prototype utilized a single quartz bar of the Babar DIRC and a cylindrical mirror placed in a mineral oil expansion volume. Commercially-available MCP-PMTs and flat-panel multi-anode PMTs with 8×8 square pixels were investigated [42–44] and showed to fulfill the FDIRC requirements.

A time-of-propagation (TOP) counter has been developed [45] to upgrade the barrel PID detector of the Belle-II experiment. The counter, currently under construction, exploits the total internal reflection of Cherenkov photons produced by charged particles traversing a thin quartz radiator. The position and arrival time of these reflected photons are measured at the radiator ends by dedicated MCP-PMTs [46,47]. The particle velocity is inferred from both the measurement of the Cherenkov angle in the radiator and the particle TOF from the interaction point. This requires MCP-PMTs with 50 ps time resolution and a spatially-segmented anode in the form of a linear array of 4×1 rectangular pixels. The TOP counter evolved to an imaging TOP (iTOP) through the addition of a spherical focusing mirror that minimizes photon spread and reduces the effects of chromatic dispersion. The MCP-PMT anode segmentation needed to be changed accordingly to a 2-dimensional array of 4×4 pixels. The MCP-PMTs developed for iTOP have also been shown to sustain photon illumination rates up to $10\ \text{MHz}/\text{cm}^2$, a value well beyond the required maximum value of about $300\ \text{kHz}/\text{cm}^2$ [48]. It is well known from previous systematic studies [49,50] that a high-rate capability is made possible through the use of MCPs with small-diameter ($10\ \mu\text{m}$) pores and low-resistivity material reducing the MCP recovery time.

Due to space limitations, the PID system of the PANDA experiment will be built with DIRC-type detectors: a barrel DIRC [51] and a disc DIRC [52] in the forward direction. The barrel DIRC is based on the Babar DIRC principle. Its requirements on time resolution (< 100 ps), spatial resolution ($5 \times 5\ \text{mm}^2/\text{pixel}$) and maximum illumination rate ($200\ \text{kHz}/\text{cm}^2$) are satisfied by MCP-PMTs that are nowadays commercially available. The disc-DirC partially reproduces the design of the iTOP detector. It however necessitates MCP-PMTs robust to photon rates exceeding $1\ \text{MHz}/\text{cm}^2$ and equipped with rectangular pixels of size $0.5\ \text{mm} \times 8\ \text{mm}$. The small dimension implies a matching footprint size of the output charge

[53–55] that will impose constraints on the MCP–PMT design and operating parameters.

Timing of internally Reflected Cherenkov photons (TORCH) [56,57] is a TOF detector proposed for the low-momentum PID upgrade of LHCb. The TORCH design is largely inspired by the concepts of the BaBar DIRC and the Belle-II iTOP detectors. To reconstruct the trajectory of the Cherenkov photons in quartz, their position and arrival time must be measured with high precision. From simulation, TORCH requires the development of MCP–PMTs with a TTS better than 50 ps for single photons and an anode segmented in 128×8 pads each $0.4 \text{ mm} \times 6.4 \text{ mm}$ in size (for a 2" square tube). As already mentioned, this fine segmentation imposes a matching charge footprint size to optimize charge sharing, readout performance, efficiency, spatial and time resolutions [58]. Commercially-available photon detectors are adequate for TORCH in terms of gain and time resolution [59]. They are not in terms of segmentation and lifetime. Consequently, the TORCH R&D activities are focused on the development of suitable photon detectors in close collaboration with industry [58,60].

A detailed discussion on the developments of dedicated readout electronics for these high-energy physics detectors is beyond the scope of the present paper. The various options that are being followed include the use of fast analogue memories [61,62]. Also under investigations is the use of a fast amplifier discriminator providing a digital output pulse with time-over-threshold measurement of the input charge [63–65]. The high illumination rates and occupancies exclude in most cases the use of more classical readout techniques like the resistive anode [66], the cross strip anode [67] and the capacitive division [68].

4.3. Recent developments

The accumulated charge densities of 1 to 10 C/cm^2 expected from the high illumination rates in Belle-II, PANDA and TORCH are well beyond the capabilities of “standard” MCP–PMTs. Some 10 years ago, these standard tubes were showing a dramatic drop in their performance at a few to a few hundreds of mC/cm^2 . The performance degradation was essentially due to ion feed-back effects that were affecting the photocathode, the multiplication gain and the time resolution. Considerable efforts were consequently dedicated to improving the MCP–PMT lifetime.

Barnyakov and Mironov [69] developed specially-treated bialkali photocathodes in combination with improved MCP scrubbing. Tests performed for the best MCP–PMT at a gain of 10^6 and high illumination rates of 2–10 MHz/cm^2 showed an increased robustness to ion feed-back up to a few C/cm^2 . However, these photocathodes have significant dark count rates of up to 100 kHz/cm^2 .

The route followed by the Belle-II Collaboration involved the use of a thin (5–10 nm) aluminium oxide film acting as an ion barrier [70] in MCP–PMTs with Chevron configuration. The film may be placed between the photocathode and the first MCP, with however a strong reduction of the photoelectron collection efficiency from 60 to 35%. The preferred solution was found by placing the film between the first and second MCP. In addition to the film, a ceramic insulator was implemented to seal the anode region of the tube with respect to the cathode region [71]. This followed the speculation that neutral molecular gas molecules are desorbed during the multiplication process in the MCP. These molecules may possibly migrate toward the photocathode and deteriorate it through direct reactions. The outcome of the above two measures is illustrated in Fig. 6. For most of the tube prototypes, the lifetime was seen to extend to about 2–3 C/cm^2 .

A recent and innovative approach has been proposed and realized by Beaulieu et al. [72]. Standard MCPs undergo an additional atomic layer deposition (ALD) process that substantially increases their gain and improves their stability as a function of extracted charge. The

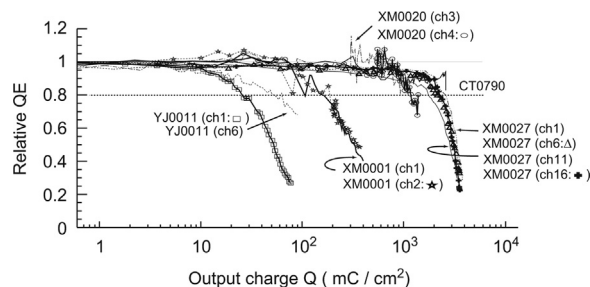


Fig. 6. Relative quantum efficiency at 400 nm as a function of the integrated output charge density for MCP–PMTs developed by the Belle-II Collaboration [71].

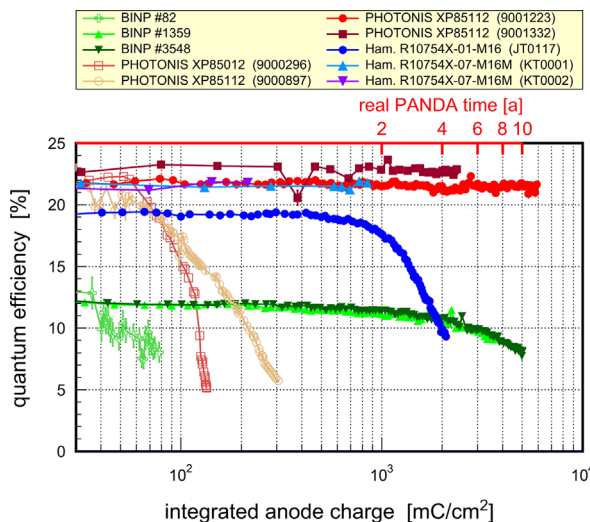


Fig. 7. Quantum efficiency at 400 nm as a function of the integrated output charge density for MCP–PMTs developed by the PANDA Collaboration [73].

process is subdivided in three steps with the successive depositions of a resistive layer, a secondary emission layer and an electrode layer. Since the layers are very different in nature, it is possible to independently optimize their performance. This ALD process has been applied to MCP–PMTs developed by the PANDA Collaboration [73,74]. Fig. 7 displays the quantum efficiency of various MCP–PMTs as a function of the integrated anode charge density. Those tubes treated with ALD exhibit fully stable quantum efficiency for integrated output charge densities exceeding 5 C/cm^2 . It is interesting to note that the left-hand curves refer to state-of-the-art MCP–PMTs that were available in 2011. For these tubes, the quantum efficiency at 400 nm dropped by a factor of four to five for an integrated output charge density between 100 and 300 mC/cm^2 . Following this breakthrough, the ALD technique has been introduced in the production of MCP–PMTs for iTOP. It has also been successfully applied in MCP–PMT prototype tubes for TORCH [60].

The same ALD technology allows the use of MCP substrate materials different from lead glass. The approach pursued by Siegmund et al. [75–77] involves the development of large-format microcapillary arrays made of borosilicate glass. A number of arrays up to 20 cm in size and $20 \mu\text{m}$ pore diameter have been fabricated and tested. They show optimal properties similar to conventional MCPs.

Other MCP material developments will be finally mentioned for completeness. The performance of amorphous silicon-based MCPs has dramatically improved over the last few years [78,79]. Such MCPs offer the advantageous possibility of monolithic fabrication on readout electronics. With the application of an ALD process, a gain of 150 has been achieved for a channel aspect ratio of 11.5:1. Anodic alumina has also been investigated [80,81]. Despite some

attractive features, this type of material has so far not produced reliable and viable MCPs.

5. Conclusions and perspectives

The MCP concept is old but the technology is still evolving and improving. The most spectacular progress is on MCP lifetime that has been extended by orders of magnitude. For high-energy physics applications, the latest trend goes towards finer anode segmentation of MCP-PMT tubes and consequently towards higher channel counts. This together with the required high speed and high signal-to-noise ratio represents a challenge for the associated readout electronics. The perspective of much larger area coverage is also appealing.

Much more has been and is taking place than what has been covered in the present paper. This (partially historical) review was actually a mix between an overview, a tutorial and a highlight from the viewpoint of a modest MCP user. The selection criteria were a combination of:

- the author's past and current activities and interests;
- those MCP-related developments coming from relatively old, new and near-future R&D and experiment projects;
- topics which were covered in other oral or poster presentations during this Conference;
- topics the illustrations of which were easily accessible, directly via authors, publications and web sites.

References

- [1] P.T. Farnsworth, Electron Multiplier, US Patent 1,969,399, 1930.
- [2] H. Bruining, *Physics and Applications of Secondary Electron Emission*, Pergamon Press, London, 1954.
- [3] R.L. Green, K.B. Blodgett, *Journal of the American Ceramic Society* 31 (1948) 89.
- [4] K.B. Blodgett, *Journal of the American Ceramic Society* 34 (1951) 14.
- [5] P.K. Oshchekpov, et al., *Pribory Tekhn. Eskper.* 4 (1960) 89; P.K. Oshchekpov, et al. (English translation in), *Instruments and Experimental Techniques* 4 (1960) 611.
- [6] L. Heroux, H.E. Hinteregger, *Review of Scientific Instruments* 31 (1960) 280.
- [7] G.W. Goodrich, W.C. Wiley, *Review of Scientific Instruments* 32 (1961) 846.
- [8] G.W. Goodrich, W.C. Wiley, *Review of Scientific Instruments* 33 (1962) 761.
- [9] G. Eschard, B.W. Manley, *Acta Electronica* 14 (1) (1971) 19.
- [10] J.L. Wiza, *Nuclear Instruments and Methods* 162 (1979) 587.
- [11] J.G. Timothy, *ISSI Scientific Reports Series* 9 (2010) 365.
- [12] J. Adams, B.W. Manley, *IEEE Transactions on Nuclear Science* NS13 (1966) 88.
- [13] K.C. Schmidt, C.F. Hendee, *IEEE Transactions on Nuclear Science* NS13 (1966) 100.
- [14] W.M. Sackinger, J.M. Johnson, *Advances in Electronics and Electron Physics* 28A (1969) 507.
- [15] M.C. Johnson, *Review of Scientific Instruments* 40 (1969) 311.
- [16] M.I. Green, et al., *Nuclear Instruments and Methods* 99 (1972) 445.
- [17] E.H. Eberhardt, *IEEE Transactions on Nuclear Science* NS28 (1981) 712.
- [18] A.J. Guest, *Acta Electronica* 14 (1) (1971) 79.
- [19] P.B. Soul, *Nuclear Instruments and Methods* 97 (1971) 555.
- [20] I.P. Csorba, *Image Tubes*, Howard W. Sams & Co., Inc, 1985.
- [21] Nikon MicroscopyU, *Fundamentals of Digital Imaging*, (<http://www.microscopyu.com/articles/digitalimaging/digitalintro.html>).
- [22] J.-C. Rebuffie, *Acta Electronica* 27 (3–4) (1987) 165.
- [23] N. Koshida, M. Hosobuchi, *Review of Scientific Instruments* 56 (1985) 1329.
- [24] M. Fouassier, et al., *Acta Electronica* 20 (1977) 369.
- [25] D.J. Ruggieri, *IEEE Transactions on Nuclear Science* NS19 (1972) 74.
- [26] T.H. Hoenderken, et al., *Journal of Vacuum Science and Technology B* 19 (2001) 843.
- [27] R.E. Anson, et al., *Nuclear Instruments and Methods A* 265 (1988) 33.
- [28] J. Alitti, et al., *Nuclear Instruments and Methods A* 283 (1989) 646.
- [29] S. Aoki, et al., *Nuclear Instruments and Methods A* 344 (1994) 143.
- [30] E. Radicioni, *Nuclear Physics B: Proceedings Supplements* 85 (2000) 95.
- [31] C. Angelini, et al., *Nuclear Instruments and Methods A* 289 (1990) 342.
- [32] C. Angelini, et al., *Nuclear Instruments and Methods A* 289 (1990) 356.
- [33] G. Haefeli et al., *this Conference*.
- [34] J.-P. Boutot, G. Piétri, *IEEE Transactions on Electron Devices* ED17 (1970) 493.
- [35] G.W. Fraser, *Nuclear Instruments and Methods A* 291 (1990) 595.
- [36] S. Korpar, et al., *Nuclear Instruments and Methods A* 595 (2008) 169.
- [37] H. Kichimi, et al., *Nuclear Instruments and Methods A* 325 (1993) 451.
- [38] A. Lehmann, et al., *Nuclear Instruments and Methods A* 595 (2008) 173.
- [39] S. Hirose, *Nuclear Instruments and Methods A* 766 (2014) 163.
- [40] I. Adam, et al., *Nuclear Instruments and Methods A* 538 (2005) 281.
- [41] J. Va'vra, et al., *Nuclear Instruments and Methods A* 718 (2013) 541.
- [42] C. Field, et al., *Nuclear Instruments and Methods A* 518 (2004) 565.
- [43] C. Field, et al., *Nuclear Instruments and Methods A* 553 (2005) 96.
- [44] J. Va'vra, et al., *Nuclear Instruments and Methods A* 572 (2007) 459.
- [45] K. Nishimura, *Nuclear Instruments and Methods A* 639 (2011) 177.
- [46] K. Inami, *Physics Procedia* 37 (2012) 683.
- [47] S. Hirose, *this Conference*.
- [48] K. Inami, et al., *Nuclear Instruments and Methods A* 592 (2008) 247.
- [49] G.W. Fraser, et al., *Nuclear Instruments and Methods A* 306 (1991) 247.
- [50] A.S. Tremsin, et al., *Nuclear Instruments and Methods A* 379 (1996) 139.
- [51] M. Hoek, et al., *Nuclear Instruments and Methods A* 766 (2014) 9.
- [52] O. Merle, et al., *Nuclear Instruments and Methods A* 766 (2014) 96.
- [53] A.S. Tremsin, O.H.W. Siegmund, *Review of Scientific Instruments* 70 (1999) 3282.
- [54] G.J. Price, G.W. Fraser, *Nuclear Instruments and Methods A* 474 (2001) 188.
- [55] X. Zhang, et al., *Review of Scientific Instruments* 80 (2009) 033101.
- [56] M.J. Charles, R. Forty, *Nuclear Instruments and Methods A* 639 (2011) 173.
- [57] M.W.U. van Dijk, et al., *Nuclear Instruments and Methods A* 766 (2014) 118.
- [58] T. Gys, et al., *Nuclear Instruments and Methods A* 766 (2014) 171.
- [59] L. Castillo García et al., *Proceedings of the 14th ICATPP Conference*, World Scientific, 2014, 633.
- [60] T.M. Conneely, et al., *Nuclear Instruments and Methods A* 732 (2013) 388.
- [61] C. Beigbeder, et al., *Nuclear Instruments and Methods A* 718 (2013) 186.
- [62] L.L. Ruckman, G.S. Varner, *Nuclear Instruments and Methods A* 602 (2009) 438.
- [63] R. Gao, et al., *Journal of Instrumentation* 9 (2014) C02025.
- [64] J.S. Lapington, T.M. Conneely, *Nuclear Instruments and Methods A* 648 (2011) S186.
- [65] M. Despeisse, et al., *IEEE Transactions on Nuclear Science* NS58 (2011) 202.
- [66] M. Lampton, C.W. Carlson, *Review of Scientific Instruments* 50 (1979) 1093.
- [67] O. Siegmund, et al., *Nuclear Instruments and Methods A* 610 (2009) 118.
- [68] J.S. Lapington, *Nuclear Instruments and Methods A* 695 (2012) 410.
- [69] M.Y.u. Barnyakov, A.V. Mironov, *Journal of Instrumentation* 6 (2011) C12026.
- [70] N. Kishimoto, et al., *Nuclear Instruments and Methods A* 564 (2006) 204.
- [71] T. Jinno, et al., *Nuclear Instruments and Methods A* 629 (2011) 111.
- [72] D.R. Beaulieu, et al., *Nuclear Instruments and Methods A* 607 (2009) 81.
- [73] A. Lehmann, et al., *Nuclear Instruments and Methods A* 766 (2014) 138.
- [74] F. Uhlig et al., *this Conference*.
- [75] O.H.W. Siegmund, et al., *Nuclear Instruments and Methods A* 639 (2011) 165.
- [76] O.H.W. Siegmund, et al., *Nuclear Instruments and Methods A* 695 (2012) 168.
- [77] O.H.W. Siegmund et al., *this Conference*.
- [78] A. Franco, et al., *Nuclear Instruments and Methods A* 695 (2012) 74.
- [79] A. Franco, *this Conference*.
- [80] K. Delendik, et al., *Nuclear Physics B: Proceedings Supplements* 125 (2003) 394.
- [81] D. Drobychev, et al., *Nuclear Instruments and Methods A* 567 (2006) 290.